CrossMark

Impact of Reversed Austenite on the Impact Toughness of the High-Strength Steel of Low Carbon Medium Manganese

GUANQIAO SU,[1] XIUHUA GAO,[1,3] DAZHENG ZHANG,[1] LINXIU DU,[1] JUN HU,[1] and ZHENGUANG LIU[2]

1.—The State Key Laboratory of Rolling and Automation, Northeastern University, Shenyang 110819, China. 2.—School of Materials Science and Engineering, Jiangsu University of Science and Technology, Zhenjiang 212003, China. 3.—e-mail: gaoxiuhua@126.com

We elucidate the relationship between the volume fraction of austenite and the Charpy impact toughness in a medium-Mn steel in terms of microstructural evolution with impact temperature. Different from retained austenite in the matrix after direct quenching, sub-micron lath-shaped morphology-reversed austenite in medium-Mn steel was produced by intercritical annealing. We found that reversed austenite steadily affected the fracture mode; only ductile fractures and dimples decreased with decreasing impact temperature. After the impact fracture test, the content of reversed austenite in the matrix increased slightly with a decreasing impact temperature due to the stability of the austenite grains caused by recrystallization of α' martensite. Reversed austenite slightly decreased during the impact process with a decreasing impact temperature.

INTRODUCTION

Many recent reports have elucidated the reversed austenite phase into medium-Mn high-strength steel by intercritically annealing to balance the comprehensive mechanical properties.[1–5] For cryogenic applications in offshore structures (such as the sheet pile of drilling platforms in the polar regions), medium-Mn steel exhibits excellent low-temperature toughness (the impact absorbed energy is $\sim$ 40 J/cm^2 at $-$ 196°C) and has an obvious price advantage compared with traditional Fe-Ni martensitic steel.[6] For reversed austenite, the key factors of its stability, combined with the incorporation of various alloy elements (such as Mn, Ni, Si and Al), guarantee that medium manganese steel can be safely used in low-temperature environments.[7–15] These elements may increase the depth and size of dimples by producing sufficient plastic deformation of ductile and stable austenite. Thus, the TRIP (transformation-induced plasticity) effect is maintained at higher strains, and the unit crack path is reduced. Liu et al.[15] controlled the strength and impact toughness by hot rolling and annealing at 630°C and 650°C, the strain rate of the tested steels was 1.67×10^{-3} s^{-1}, and the steels exhibited a stable change in toughness and energy absorption

during impact at $-$ 60°C (81.2 J and 114.2 J with a ductile fracture mode, respectively). The decline in the degree of impact-absorbed energy did not decrease quickly with a decrease in impact temperature; the decreasing values, from 20°C to $-$ 60°C, were around 10–50 J, respectively. Han et al.[16] reported a "prior austenite grain boundary break-up" mechanism and compared the intergranular cracking propagated between direct annealing and cold rolling before annealing, and showed that it improved the toughness of medium-Mn steel. These studies discussed the influence of reversed austenite on toughness controlled by the type of rolling and heat treatment. However, the stability of reversed austenite with respect to impact temperature has never been reported.

Because medium manganese steel has good application prospects in low-temperature environments, the relationship between reversed austenite and impact absorbed energy should be established. In the current experiments, the microstructure of low-C medium-Mn steel with sub-micron lath-shaped morphology-reversed austenite was produced using an intercritical annealing process, and the effects of reversed austenite in enhancing toughness, in relation to the stability of austenite grains, were explored. We used various impact tests at different

lower temperatures to determine the relationship between impact toughness and metastable reversed austenite. A new relationship between toughness and loss in the volume fraction of reversed austenite (at different temperatures) is presented.

EXPERIMENTAL PROCEDURES

The chemical composition of the designed medium manganese steel specimen is Fe-0.045C-0.23Si-5.08Mn-0.39Cr-0.32Ni-0.3Cu-0.2Mo-0.011Al-0.005P-0.003S (in mass%). The presence of chromium can produce an offset effect on the adverse impact of manganese to increase corrosion resistance.[17–20] The steel was melted using a vacuum induction furnace. The steel was cast into ingots and forged into 140-mm-thick billets. The billets were homogenized at 1200°C for 1 h and rolled into 30-mm-thick plates at 960°C in nine passes and completely hot rolled at 900°C. The hot-rolled steel plate was quenched immediately with water to room temperature. The plates were reheated to 650°C for 30 min and air-cooled to room temperature.

Coupons were carried out parallel to the rolling direction of plates for Tensile and Charpy impact tests. According to ISO 6892-1:2009, three tensile specimens (30 mm long with 6 mm diameter) were used to measure tensile properties using a Shimadzu AG-X universal testing machine at room temperature and a crosshead speed of 3 mm/min.[21] The strain rate was 1.67×10^{-3} s^{-1}, calculated based on the loading rate and specimen length. Standard Charpy v-notch specimens $(10 \times 10 \times 55$ mm$^3)$ measured using an Instron Dynatup 9200 series drop weight impact tester at 0°C, − 20°C, − 40°C and − 60°C consistent with the ASTM E23 specification. Three replicate tests were used for each impact test, and the final result was the average value of the tests.

The microstructure morphology of the steel was characterized using an FEI Tecnai G^{2}F20 transmission electron microscope (TEM). The XRD measurements were conducted with a D/max 2400 x-ray diffraction (XRD) system with a Cu$_{K\alpha}$ ($\lambda = 0.154$ nm) target and a step size of 0.04°. The Charpy impact fracture specimens were observed with FEI Quanta 600 scanning electron microscope (SEM) and the EBSD specimens prepared from the fracture area by electropolishing in a $\sim 87.5\%$ absolute ethyl alcohol and $\sim 12.5\%$ perchloric acid mixture to remove the strain layer on the surface. A Zeiss Ultra 55 scanning electron microscope (FE-SEM) equipped with an EBSD attachment was used to obtain clear morphology with a step size of 0.1 μm. The content of reversed austenite was determined using the integrated intensities of $(200)\gamma$, $(220)\gamma$, $(311)\gamma$, $(200)\alpha$ and $(211)\alpha$ peaks in Eq. 1[22] through the XRD patterns.

$$V_\gamma = 1.4I_\gamma/(I_\alpha + 1.4I_\gamma) \qquad (1)$$

RESULTS AND DISCUSSION

Bright- and dark-field TEM images of the designed steel are presented in Fig. 1a and b, respectively. Some reversed austenite (see the red circle line in Fig. 1a) can be found on the boundaries of α laths, which can be confirmed by the SAED pattern (Fig. 1c), and their thickness is between 100 nm and 250 nm, while the thickness of the α laths is between 200 nm and 500 nm. The γ phase presents a lath-shaped microstructure along the boundaries of the α laths. The content of reversed austenite was determined using the Thermo-Calc software combined with the TCFE6 database and the XRD patterns for thermodynamic calculation in equilibrium (Fig. 1d), and the volume fraction of retained austenite and reversed austenite was 0.6% and 22% for direct quenching and annealing, respectively. It is noted that the volume fraction of austenite is rather subjective in our results based on the calculation in Hu's report;[23] the calculation in this article will cause some errors in the results. The volume fraction of austenite is only for reference here, and the error value may be about 2–3% from the in situ synchrotron x-ray diffraction (SYXRD) result.

The crystallographic characteristics of the designed steel analyzed by EBSD are presented in Fig. 2. In the image quality (IQ) map with a grain boundary misorientation distribution, the blue and red lines represent high misorientation boundaries of 15° and larger than 15° and low misorientation boundaries of 2°–15°, respectively.[24,25] The water-quenched steel consists of small packets with fine laths, and there was a high fraction of high misorientation boundaries (Fig. 2a). When the coupon was annealed, the laths became coarse and the packet boundaries had high misorientation (Fig. 2b). Some rod- and globular-shaped structures with yellow filling along the grain boundaries (arrowed in Fig. 2b) have a face-centered cubic structure, meaning that the reversed austenite appeared. For the annealed steel specimens, the coupons were cut from the fracture zone after the low-temperature impact fracture. The IQ map and grain boundary misorientation distribution of steel after the 0°C impact fracture showed that the laths became fine again (Fig. 2c), while the high misorientation rate decreased. After the − 60°C impact fracture, the high misorientation and low misorientation were similar to the directly quenched coupons (Fig. 2d).

The IPF map (Fig. 3) reveals the orientation distribution at various states. The hot rolled deformation structure after direct quenching has a relatively concentrated orientation distribution; most of the area of Fig. 3a is blue and close to [111]. However, after the annealing treatment (see Fig. 3b), the orientation distribution shifts to a dispersion distribution state, and a certain number of the grains oriented with the [111] direction
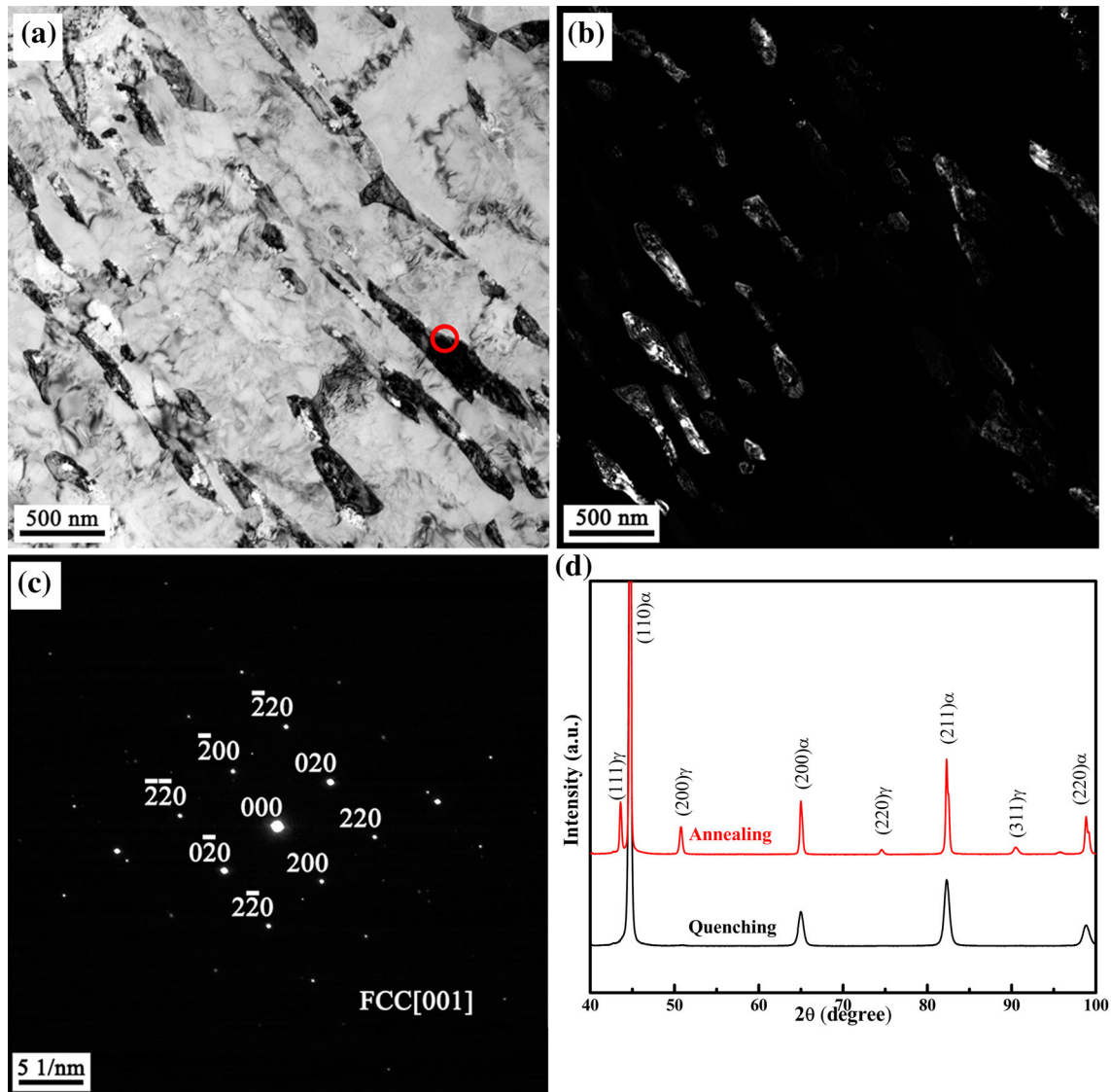
Fig. 1. (a)-(c) TEM micrographs of coupons annealed at 650°C for 30 min of bright-field image, dark-field image and SAED pattern of austenite; (d) XRD patterns of quenching and annealing coupons.

gradually inclined to the [101] direction, indicating that the number of the orientation with the [111] direction decreased. Compared to direct quenching, the toughness of the annealed steel increased, but the strength decreased. After the 0°C impact fracture (Fig. 3c), toughness decreased in areas of concentrated orientation distribution and increased again when stress appeared and the degree of the started slip system increased. Combined with the XRD patterns (Fig. 4a and b) and the − 60°C impact fracture (Fig. 3d), compared to the 0°C impact, the degree of $\gamma \rightarrow \alpha$ decreased after the − 60°C impact fracture. With decreasing impact temperature, the reversed austenite in the matrix increased slightly because of the stability of the austenite grains through the recrystallization of α' martensite, and the reversed austenite decreased slightly during the impact process with decreased impact temperature.

The mechanical properties are presented in Fig. 4b and c; the Charpy absorbed energy values were 232 J (0°C), 230 J (− 20°C), 220 J (− 40°C) and 192 J (− 60°C); the yield and tensile strength of the tested steel were 703 MPa and 827 MPa. Figure 4b also shows the relationship between the volume fraction of austenite in a matrix and the impact-absorbed energy for different impact temperatures. As shown in Fig. 4a, the volume fractions of austenite corresponding to different impact temperatures were calculated as 7.6%, 8.2%, 11.2% and 12.2%, respectively. The change in the degree of impact-absorbed energy relative to impact temperatures ranging from 0°C to − 40°C was very small; the difference was ∼ 2–10 J. However, as the impact temperature dropped to − 40°C, the impact-absorbed energy showed a significant decline (∼ 28 J). In addition, the difference in the
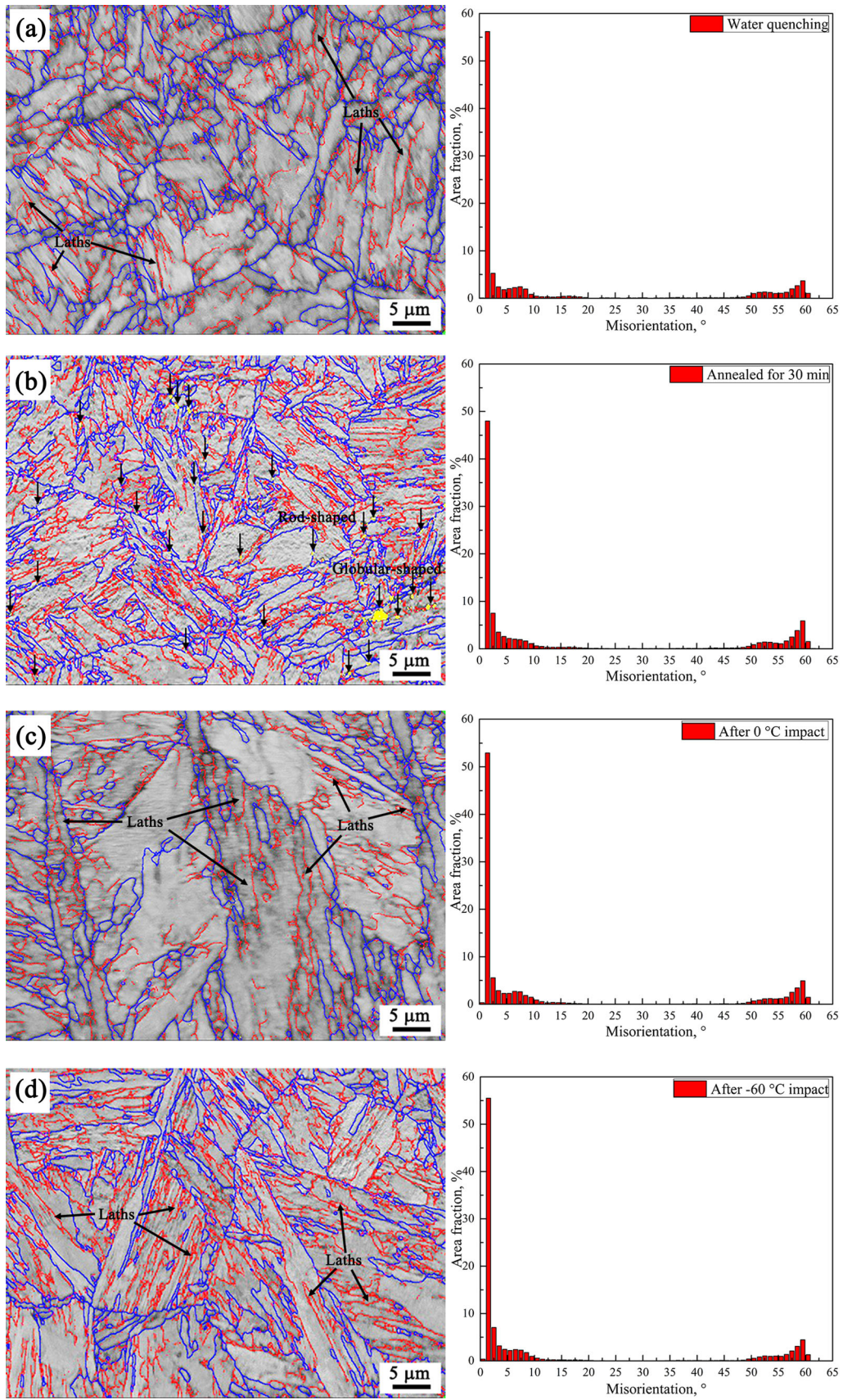
◄ Fig. 2. Crystallographic characteristics of tested steels analyzed by EBSD: (a) IQ map and GB misorientation distribution of steel after water quenching; (b) IQ map and GB misorientation distribution of steel annealed at 650°C for 30 min; (c) IQ map and GB misorientation distribution of steel (annealed) after 0°C impact fracture; (d) IQ map and GB misorientation distribution of steel (annealed) after -60°C impact fracture.

austenite volume fraction between − 40°C and − 60°C was smaller than the previous ones. These results imply that the extent of deformation-induced metastable austenite to martensite decreased with the decreasing impact temperature. Therefore, it is reasonable to infer that the TRIP effect has a tendency of rapidly decreasing and then steadily decreasing until the ductile brittle transition temperature of the tested steel is reached. Figure 5a, b, c, and d shows the SEM fracture surface after the impact fracture of the annealing coupons. The coupons from the different test temperatures were 0°C, − 20°C, − 40°C and − 60°C. All fractographs

from 0°C to − 60°C showed a ductile-fractured surface with large, fine dimples. The size of the fine dimples decreased as the impact temperature decreased because of increased stress concentrations. Generally, ductile fracture consists of three stages, namely nucleation of the voids, growth and coalescence of the voids, followed by joining with a macro- or meso-crack. This process corresponds to extensive plastic deformation, which contributed to the good impact toughness with fine dimples, while the dimple size decreased as the impact temperature decreased. Srivastava et al.[26] and Gerbig et al.[27] reported a new approach for modeling formability and predicting the properties of the constituent phases and microstructure of dual phase steels, influencing fracture resistance. From the microstructure-based fracture model in the resistance, increasing the volume fraction of martensite results in a reduction in fracture resistance. Similar to our experiments, the variations of austenite volume fraction after impact tests at different test temperatures are different. After the
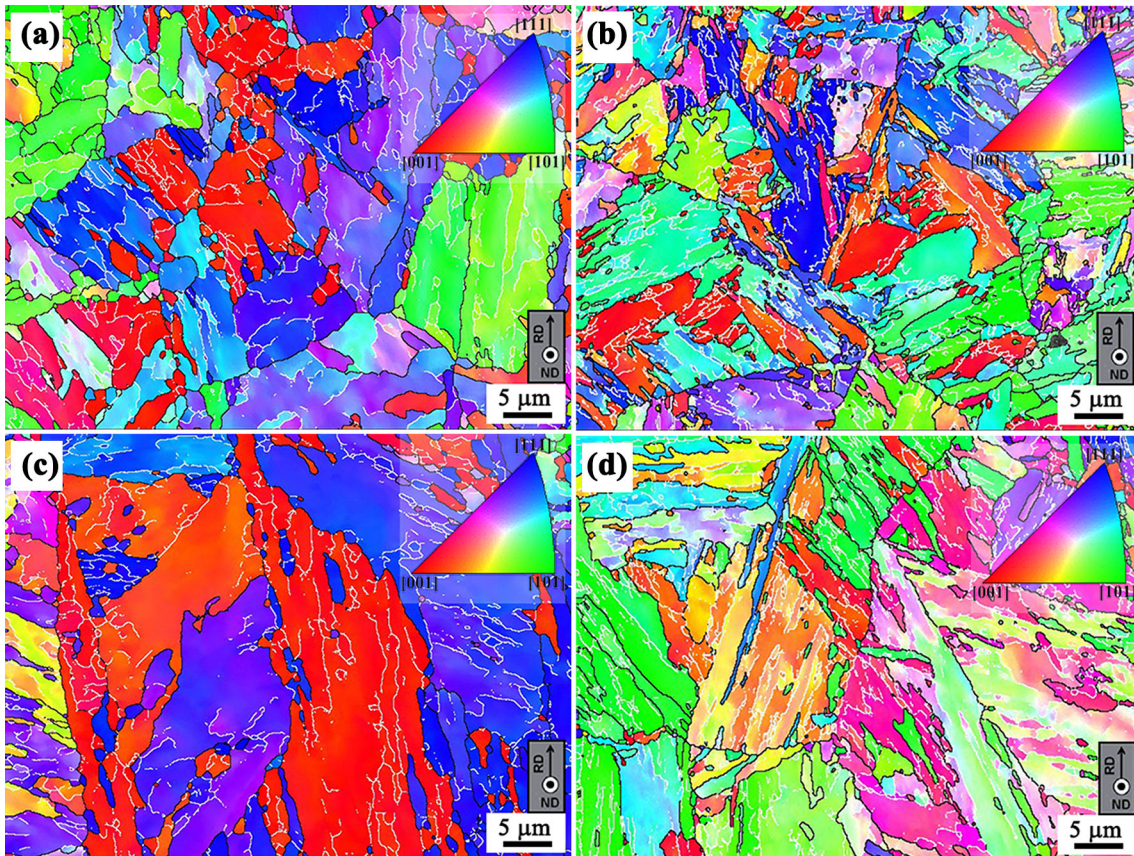

Fig. 3. EBSD analysis results of the tested steel: (a) orientation map of steel after water quenching; (b) orientation map of steel annealed at 650°C for 30 min; (c) orientation map of steel (annealed) after 0°C impact fracture; (d) orientation map of steel (annealed) after − 60°C impact fracture.
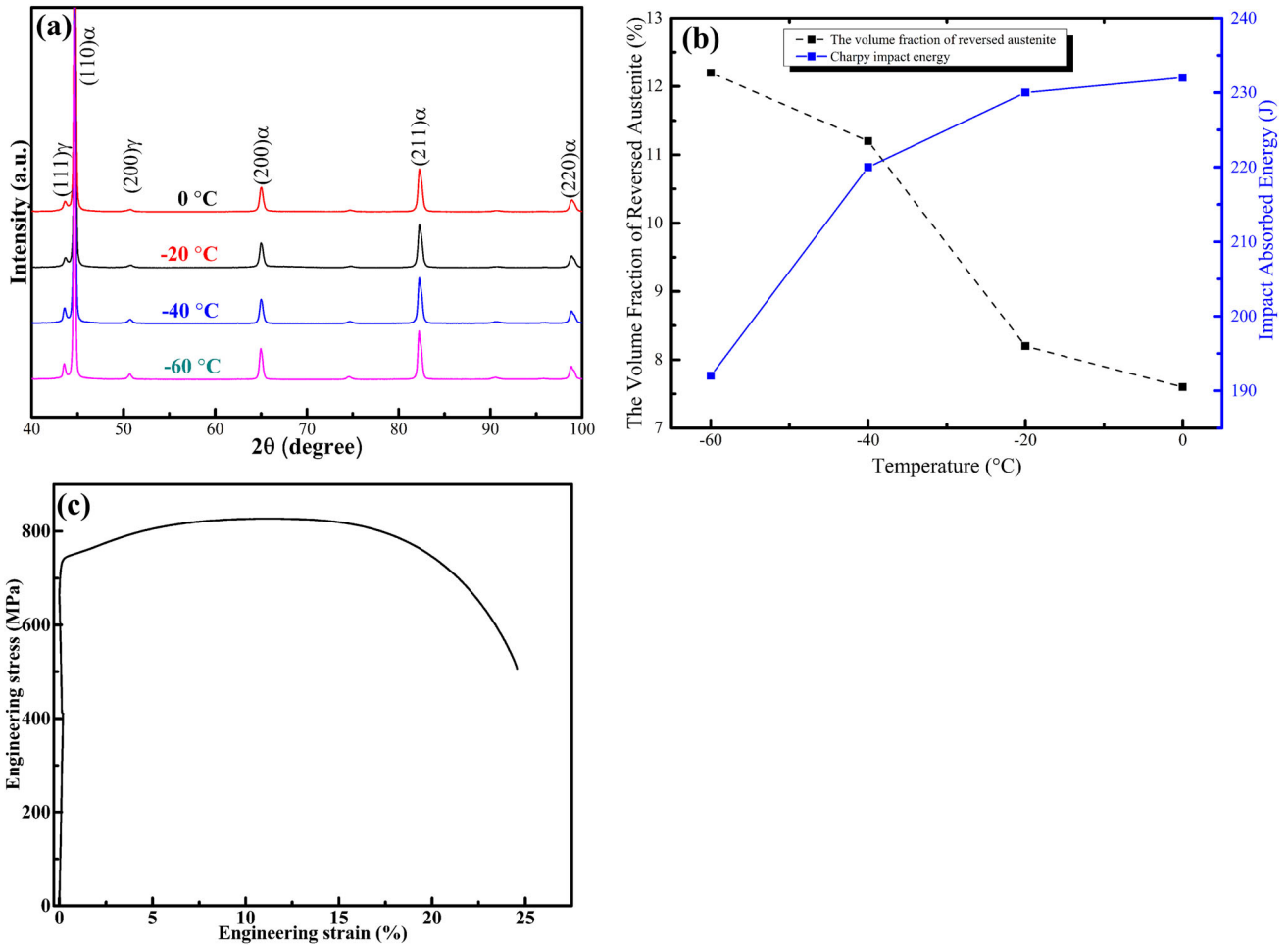
Fig. 4. (a) XRD patterns of annealed coupons from fracture zones after impact fracture at various temperatures; (b) volume fractions of austenite and Charpy impact energy as functions of impact temperature; (c) engineering stress-strain curve of tested steel.

impact tests, the retained martensite of the tested steels increased with a constantly decreasing test temperature. As a result, the fracture resistance decreased and the dimple size presented a decreasing trend.

CONCLUSION

For obtaining the effect of reversed austenite on the impact toughness of high-strength low-carbon medium-manganese steel at different impact temperatures, the conclusions were as follows:

1. The experimental steel consisted of sub-micro lath-shaped reversed austenite ($\sim$ 100–250 nm) along martensite laths after intercritically

annealing at 650°C for 30 min. In addition, the volume fraction of austenite was increased from 0.6% (directly quenched) to 22% (intercritically annealed) according to a conventional calculation method.

2. Through the impact tests under the different temperatures, reversed austenite steadily affected the fracture mode and only showed that the size of dimples decreased as the impact temperature decreased.

3. The toughness of the tested medium-manganese steel exhibited a slight change (from 232 J to 192 J) at different impact temperatures from 0°C to − 60°C. In addition, the volume fractions of reversed austenite and the Charpy impact
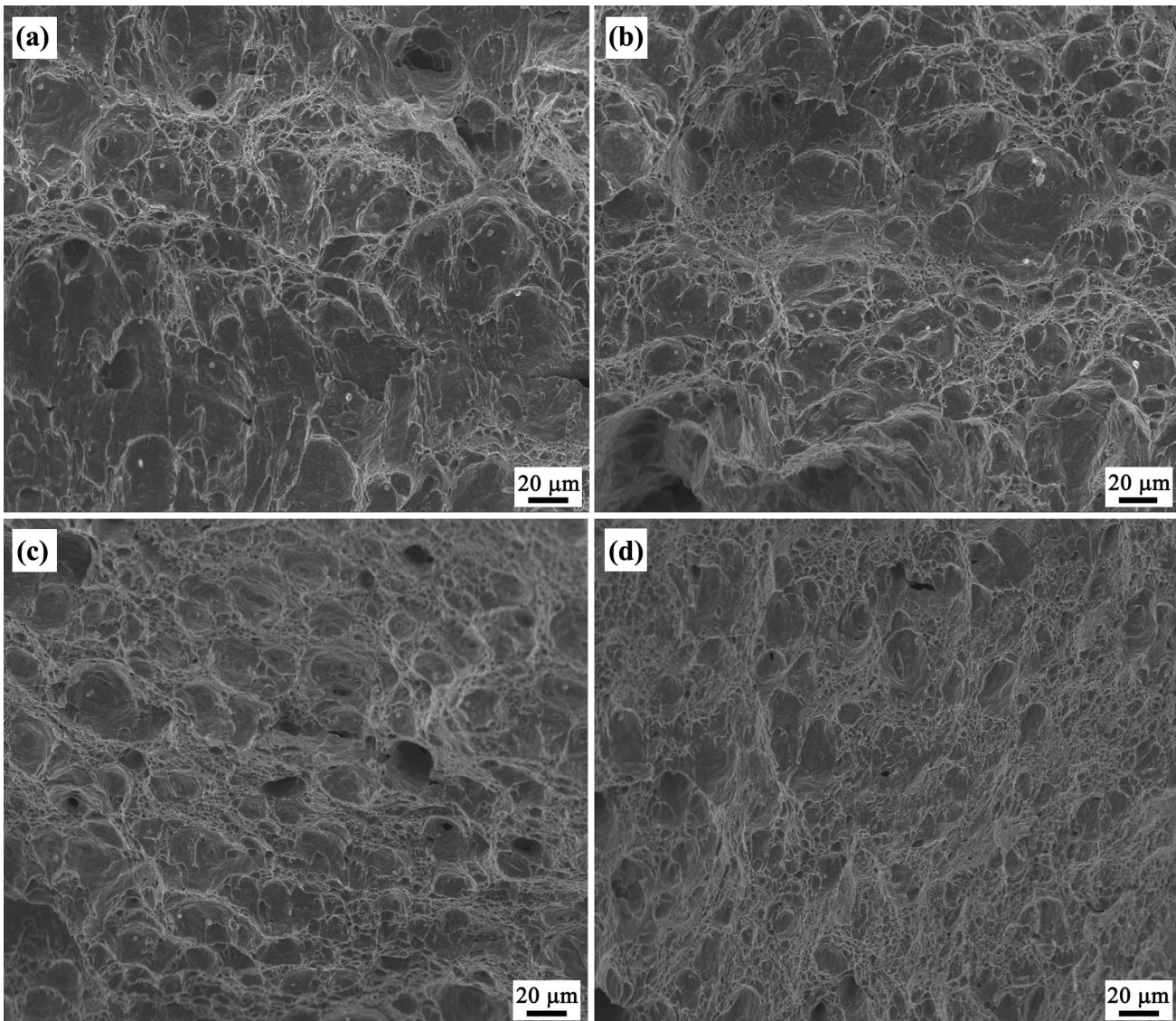
Fig. 5. SEM fractographs of annealing coupons fractured at various impact temperatures: (a) 0°C; (b) − 20°C; (c) − 40°C and (d) − 60°C.

energy, as functions of impact temperature, were revealed. After the impact fracture tests, the contents of reversed austenite in the matrix increased slightly, while the impact temperature decreased.

4. The metastable austenite significantly improved the toughness of the tested steel. The TRIP effect has the tendency of decreasing rapidly and then decreasing steadily until the ductile brittle transition temperature of the tested steel is reached.

CONFLICT OF INTEREST

The authors declare that they have no conflict of interest.

REFERENCES

1. Y.-K. Lee and J. Han, *Mater. Sci. Technol.* 31, 843 (2015).
2. J. Han, S.-J. Lee, J.-G. Jung, and Y.-K. Lee, *Acta Mater.* 78, 369 (2014).
3. S. Lee, S.J. Lee, S.S. Kumar, K. Lee, and B.C.D. Cooman, *Metall. Mater. Trans. A* 42, 3638 (2011).
4. J. Hu, L.X. Du, G.S. Sun, H. Xie, and R.D.K. Misra, *Scr. Mater.* 104, 87 (2015).

5. M. Kuzmina, D. Ponge, and D. Raabe, *Acta Mater.* 86, 182 (2015).
6. K.H. Kwon, I.C. Yi, Y. Ha, K.K. Um, J.K. Choi, K. Hono, K. Oh-ishi, and N.J. Kim, *Scr. Mater.* 69, 420 (2013).
7. H. Choi, S. Lee, J. Lee, F. Barlat, and B.C.D. Cooman, *Mater. Sci. Eng., A* 687, 200 (2017).
8. B.H. Sun, F. Fazeli, C. Scott, X.J. Yan, Z.W. Liu, X.Y. Qin, and S. Yue, *Scr. Mater.* 130, 49 (2017).
9. D.W. Suh, J.H. Ryu, M.S. Joo, H.S. Yang, K. Lee, and H.K.D.H. Bhadeshia, *Metall. Mater. Trans. A* 44, 286 (2013).
10. S.J. Lee, S. Lee, and B.C.D. Cooman, *Scr. Mater.* 64, 649 (2011).
11. Q. Zhou, L.H. Qian, J. Tan, J.Y. Meng, and F.C. Zhang, *Mater. Sci. Eng., A* 578, 370 (2013).
12. B.C.D. Cooman, P. Gibbs, S. Lee, and D.K. Matlock, *Metall. Mater. Trans. A* 44, 2563 (2013).
13. G.H. Gao, H. Zhang, X.L. Gui, P.L. Luo, Z.L. Tan, and B.Z. Bai, *Acta Mater.* 76, 425 (2014).
14. R.L. Miller, *Metall. Trans.* 3, 905 (1972).
15. H. Liu, L.X. Du, J. Hu, H.Y. Wu, X.H. Gao, and R.D.K. Misra, *J. Alloys Compd.* 695, 2072 (2017).
16. J. Han, A.K. da Silva, D. Ponge, D. Raabe, S.-M. Lee, Y.-K. Lee, S.-I. Lee, and B. Hwang, *Acta Mater.* 122, 199 (2017).
17. G.Q. Su, X.H. Gao, D.Z. Zhang, C.S. Cui, L.X. Du, C. Yu, J. Hu, and Z.G. Liu, *Corrosion* 73, 1367 (2017).
18. C.M. Enloe, J.P. Singh and J.J. Coryell, in Proceedings of the International Symposium on New Developments in Advanced High-Strength Sheet Steels (Keystone, CO, USA: Association for Iron & Steel Technology, Warrendale, PA, 2017), pp. 1–10.
19. G.Q. Su, X.H. Gao, L.X. Du, D.Z. Zhang, J. Hu, and Z.G. Liu, *Int. J. Electrochem. Sci.* 11, 9447 (2017).
20. G.Q. Su and X.H. Gao, *Materials* 10, 938 (2017).
21. ISO 6892-1, Metallic Materials-tensile Testing-Part 1: Method of Test at Room Temperature (2009).
22. K. Sugimoto, N. Usui, M. Kobayashi, and S. Hashimoto, *ISIJ Int.* 32, 1311 (1992).
23. X.H. Hu, X. Sun, L.G. Hector Jr, and Y. Ren, *Acta Mater.* 132, 230 (2017).
24. J. Hu, L.X. Du, J.J. Wang, and C.R. Gao, *Mater. Sci. Eng., A* 577, 161 (2013).
25. L.Y. Lan, C.L. Qiu, D.W. Zhao, X.H. Gao, and L.X. Du, *Mater. Sci. Eng., A* 529, 192 (2011).
26. A. Srivastava, A.F. Bower, L.G. Hector Jr, J.E. Carsley, L. Zhang, and F. Abu-Farha, *Modell. Simul. Mater. Sci. Eng.* 24, 2 (2016).
27. D. Gerbig, A. Srivastava, S. Osovski, L.G. Hector Jr, and A. Bower, *Int. J. Fract.* (2017). https://doi.org/10.1007/s10704-017-0235-x.